Volume 5 | Number 11 | 7 June 2021

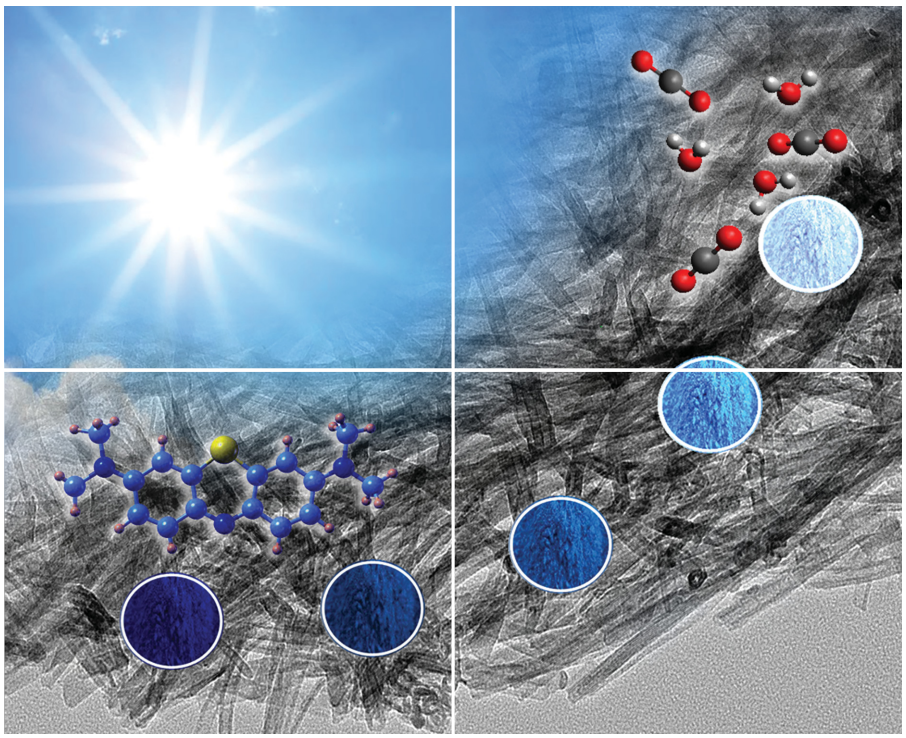

MATERIALS CHEMISTRY

FRONTIERS

CCS 中国化学会 CHINESE CHEMICAL SOCIETY

ICCAS 1956

ROYAL SOCIETY OF CHEMISTRY

rsc.li/frontiers-materials

MATERIALS CHEMISTRY FRONTIERS

CHINESE CHEMICAL SOCIETY

ROYAL SOCIETY OF CHEMISTRY

RESEARCH ARTICLE

View Article Online
View Journal | View Issue

Cite this: *Mater. Chem. Front.*, 2021, **5**, 4138

Ceria doping boosts methylene blue photodegradation in titania nanostructures†

Chiara Alberoni,[a] Isabel Barroso-Martín,[b] Antonia Infantes-Molina,[b] Enrique Rodríguez-Castellón,[b] Aldo Talon,[a] Haiguang Zhao,[c] Shujie You,[d] Alberto Vomiero *[ad] and Elisa Moretti*[a]

Received 14th January 2021,
Accepted 22nd March 2021

DOI: 10.1039/d1qm00068c

rsc.li/frontiers-materials

Ceria-doped titania photocatalysts (ceria loading 0.25–5.0 wt%) were synthesized by hydrothermal methods for water remediation. Nanotubes (CeTNT*x*) and nanoparticles (CeTNP*x*) were obtained. Ceria doping was applied to tune the electronic properties of nanostructured titania, boosting its photocatalytic activity. CeTNT nanostructures contained anatase as the only titania phase, whereas the CeTNP series consisted of both anatase and rutile polymorphs. The Ce addition induced a decrease in the energy gap, allowing enhancement of visible light harvesting. The photodegradation of methylene blue, MB, in aqueous solution was chosen to study the influence of the morphology and the ceria loading on the photocatalytic response, under UV and solar light. Both CeO_2–TiO_2 nanoparticles and nanotubes were found to be very active under UV light. The highest MB degradation rates were obtained for the 0.25 wt% CeO_2 doping, for both nanotubes and nanoparticles (0.123 and 0.146 min^{-1}, respectively), able to photodegrade completely the dye after 120 min. The two samples are stable after a 3-cycle reusability test. The photo-response under simulated solar light confirmed that doping titania with ceria allows harvesting visible light absorption, enhancing its photoactivity. A maximum efficiency of 85% under simulated sunlight at a degradation rate of 0.054 min^{-1} was obtained. Transient photoluminescence confirmed that MB acts as a charge scavenger for the composite system. These results pointed out ceria-doped titania nanostructures as a promising class of photocatalysts for the degradation of dyes and other hazardous organic compounds in wastewater.

Introduction

Water pollution constitutes an issue of major concern worldwide that not only affects the environment, but also jeopardizes human health. Moreover, it is a long-term problem since water pollution not only occurs in superficial water bodies but also reaches groundwater. This fact, together with the properties of water as a universal solvent, eases the degradation of water quality due to hazardous substances contained in wastewater effluents, such as heavy metals or organic compounds that can be non-biodegradable, highly toxic or even carcinogenic.

Among all the anthropogenic sources of water pollution, it is estimated that more than 20% comes from the textile industry, which releases between 1000 and 3000 m^3 of wastewater effluents for the processing of less than 20 tons of textiles per day.[1] These effluents usually contain high concentrations of organic and inorganic compounds due to the incomplete fixation of dyes onto the fabrics, which leads to synthetic dye contents in effluents up to 10–15% that negatively affect both the ecosystem and human health.[1] On the other hand, as well as colouring water even at concentrations below 1 mg L^{-1}, they totally or partially block sunlight penetration, thus hindering the appropriate functioning of microbiological processes in aquatic ecosystems. They can also interfere with photosynthesis, competing with living species for oxygen.[2,3]

Conventional technologies for water purification of organic contaminants such as trickling filter technology, flocculation and electrodialysis are highly energy-demanding processes with considerable operation and maintenance costs that are not effective for dye removal.[1] Adsorption is usually used in the removal of dyes from wastewater effluents and it has shown

[a] *Department of Molecular Sciences and Nanosystems, Ca' Foscari University of Venice, Via Torino 155, 30172, Venezia Mestre, Italy. E-mail: elisa.moretti@unive.it, alberto.vomiero@unive.it, alberto.vomiero@ltu.se*
[b] *Departamento de Química Inorgánica, Cristalografía y Mineralogía (Unidad Asociada al ICP-CSIC), Facultad de Ciencias, Universidad de Málaga, Campus de Teatinos, 29071 Málaga, Spain*
[c] *Qingdao University – College of Physics & State Key Laboratory of Bio-Fibers and Eco-Textiles, 308 Ningxia Road, Qingdao 266071, P. R. China*
[d] *Division of Material Science, Department of Engineering Sciences and Mathematics, Luleå University of Technology, 971 87, Luleå, Sweden*

† Electronic supplementary information (ESI) available. See DOI: 10.1039/d1qm00068c

remarkable results, especially when using nanostructured materials.[4] Nevertheless, adsorptive processes are based on the transfer of pollutants from one phase to another, so eventually dyes are not destroyed. As an alternative to achieve the complete degradation or mineralization of these compounds, advanced oxidation processes (AOPs) have emerged as a low waste generation technology consisting of chemical treatments to remove organic compounds in wastewater effluents by oxidation, taking advantage of chemical species with short lifetimes but high oxidation power, such as hydroxyl radicals. As short-lived species, OH radicals must be produced during the process through oxidizing agents such as H_2O_2 and O_3, catalysts like Fe^{2+} (Fenton process) or irradiation with UV light.[5]

In the presence of oxidants or catalysts, $OH^{\bullet}$ radicals can be initiated by photons produced by light irradiation. Titania, TiO_2, an n-type semiconductor, is the most largely employed catalyst for UV-based AOPs operating under mild conditions (atmospheric pressure and room temperature), thanks to its outstanding photocatalytic properties, as well as its low cost, non-toxicity, great chemical and thermal stability and remarkable oxidation power.[6,7] The photocatalytic performance of titania strongly depends on several parameters such as crystallinity, nanostructures' morphology, specific surface area and pore size distribution.[8–10] Thus, different strategies to modify and tune these parameters in order to obtain superior photocatalytic TiO_2-based materials have been largely investigated.

Morphology plays a key role in the transport and recombination of photogenerated charge carriers. One-dimensional nanostructures like nanotubes and nanorods present low charge carrier recombination due to the short distance for their diffusion to the surface where the reaction takes place.[11] Likewise, three-dimensional materials have emerged as promising candidates for degradation of organic compounds. Nanoparticles show outstanding performance thanks to their large surface area to volume ratio, which provides efficient diffusion pathways for pollutant molecules with the advantage that properties such as pore size, pore volume and specific surface area can be easily tuned by changes in the hydrothermal synthesis conditions used for obtaining titania nanoparticles.[12] Besides, microspheres also present high pore volume and pore size and avoid the formation of slurries after reaction in aqueous media, easing catalyst recovery.[13]

Considering that more than 40% of the total incident solar spectrum consists of visible light and only 4–5% of UV radiation,[14] great attention has been paid to broadening titania's applications as a photocatalyst under visible light irradiation through doping, with the aim of narrowing its wide band gap (3.2 eV for anatase and 3.0 eV for rutile),[15] which does not allow significantly exploiting sunlight irradiation, and decreasing its high electron–hole pair recombination rate. Doping with metal or non-metal elements can help in increasing the charge carrier lifetime by forming shallow traps slightly below (above) the conduction (valence) band. The photogenerated charge carrier recombination rate is decreased and visible light absorption is possible thanks to the defect states created in the band gap or to the introduction of energy levels in it.[16,17] Dopant efficiency towards charge carrier trapping depends on several parameters like dopant concentration and distribution, light intensity and the stability of the titania crystalline phase.[18]

Rare earth elements have been extensively studied as dopants to modify the titania crystal structure, thanks to their 4f electronic configuration.[19] When they are incorporated into a host matrix, the influence of this matrix over 4f optical transitions is negligible, as electrons at this level are shielded by the crystal field of neighbouring ions with electrons in $5s^2$ and $5p^6$ orbitals.

Doping the TiO_2 lattice with cerium ions containing 4f electrons can decrease significantly the recombination of electron–hole pairs and result in the extension of their wavelength response toward the visible region.[20,21] Among lanthanides, cerium is the most interesting element in the fields of catalysis and photocatalysis. In particular, the wide use of ceria, CeO_2, and ceria-based mixed oxides as active components for catalytic reactions, especially oxidation reactions, has been traditionally associated with its unique excellent ability to shuttle between Ce(III) and Ce(IV) states, the well-known oxygen storage capacity (OSC), allowing CeO_2-based catalysts and photocatalysts to act as oxygen buffers and thus promoting reductive and oxidative activity.[22–24] The ability of Ce^{3+} to oxidize to Ce^{4+} leads to high oxygen mobility, which in turn leads to strong catalytic potential.[17,25,26] The theoretical band gap of CeO_2 is about 6.0 eV; nevertheless, its experimental band gap is around 3.0–3.4 eV, a value very close to those of TiO_2 and ZnO,[27] the two most employed semiconductors in photocatalysis. Most probably this is due to the O 2p → Ce 4f transition, even though the origin of this reduced band gap is still controversial.[28]

Introduction of metal ions into the CeO_2 lattice can increase the density of oxygen vacancies and potentially improve the catalytic performance of CeO_2-supported metal catalysts by changing the physical and chemical properties of the supports.[29,30] The preparation of CeO_2–TiO_2 systems could reduce the band gap of pure titania, improve charge separation and/or hinder the e^-/h^+ recombination due to the novel structures and interfacial charge transfer, resulting in a potentially enhanced photocatalytic degradation efficiency.[31,32] In fact, previous research carried out by Xu *et al.*[33] associated the enhancement in the photocatalytic activity of cerium doped titania in formaldehyde degradation with the suppression of electron–hole recombination by means of electron trapping at Ce^{4+} sites. Likewise, Li *et al.*[34] also demonstrated the improved photocatalytic performance of sol–gel synthesized Ce^{3+}–TiO_2 catalysts in the photodegradation of 2-mercaptobenzothiazole in aqueous suspension with significant absorption in the visible region, suggesting that the existence of sub-energy levels in these structures may eliminate electron–hole pairs and therefore enhance their photocatalytic activity.

In the present work, nanostructured TiO_2 samples containing different CeO_2 loadings (ranging from 0.25 to 5.0 wt%) were synthesized by using hydrothermal methods in order to obtain two different nanoscale morphologies: nanotubes and nanoparticles. Their activity was evaluated in the methylene blue (MB) photodegradation at R.T. and atmospheric pressure, both under UV and solar light irradiation, and correlations between

the photocatalytic activity and physicochemical and optical properties of the nanomaterials were made.

Results and discussion

Physicochemical and optical characterization

Phase identification of pure and ceria-titania nanotubes, pure and ceria-titania nanoparticles and commercial P25 titania (used for comparison purposes) was performed by X-ray diffraction, and diffraction patterns are displayed in Fig. 1(a) and 2(a).

For all the CeTNT*x* (ceria-titania nanotube) samples, the characteristic peaks of the anatase phase emerged at $2\theta = 25.5^\circ$, 37.9°, 48.1° and 54.7°, in agreement with the values of the standard card (database PDF 73-1764).

No cerium-based phases were detected, neither in the samples with very low CeO_2 contents (0.25, 0.5, 1.0 wt%), undetectable as they are below the XRD detection limit, nor in the samples with higher ceria loadings (2.5 and 5.0 wt%), most probably due to the very highly homogeneous dispersion of cerium species in the titania matrix, or the formation of very small ceria particles decorating titania structures. This result is also confirmed by Raman spectroscopy (Fig. S1a, ESI†), in which no ceria phase is detected and peaks only from anatase are visible.[35] Even though the ionic radius of Ce^{4+} (0.97 Å) is much larger than that of Ti^{4+} (0.68 Å),[36] the introduction of cerium ions into the TiO_2 lattice, with some deformations on the lattice, and the formation of Ce–Ti solid solution, $Ce_xTi_{1-x}O_2$, cannot be discarded. It has been suggested that, for quite low Ce concentrations, the incorporation of Ce^{4+} into the anatase lattice could take place, while at higher Ce loadings (usually ≥ 5 mol%, corresponding to *ca.* 13 wt%) the anatase lattice is saturated and the formation/separation of amorphous ceria and/or ceria nucleation can occur, accompanied by an increase of TiO_2 anatase crystallite size and the limitation of the value of anatase cell volume.[37] The highest Ce concentration studied (5.0 wt%) is below the threshold for separation of amorphous ceria and/or nucleation of microcrystalline ceria. As for the TNP and CeTNP*x* samples, well resolved reflections at 2θ values of 25.5°, 38.0°, 48.1° and 54.7°, corresponding to the characteristic pattern of the anatase polymorph (PDF 73-1764), and less intense peaks related to the rutile polymorph at 2θ values of 36.0° and 54.1° (PDF 21-1276) were observed. No peaks related to cerium-based phases were detected, most probably due to the high dispersion of cerium species into the titania matrix even with a 5.0 wt% CeO_2 loading. Semi-quantitative analysis indicates that about 80% of TiO_2 present in these samples is the anatase phase and the remaining 20% the rutile polymorph, comparable with the crystalline composition of the commercial P25 titania benchmark. These results are confirmed by Raman spectroscopy (Fig. S1b, ESI†), which indicates the presence of both anatase and rutile phases.[35]

The estimated anatase mean crystal size, calculated by the Scherrer equation, was approximately 18 nm for all the samples of the CeTNT*x* series and 32 nm for the CeTNP*x* series.

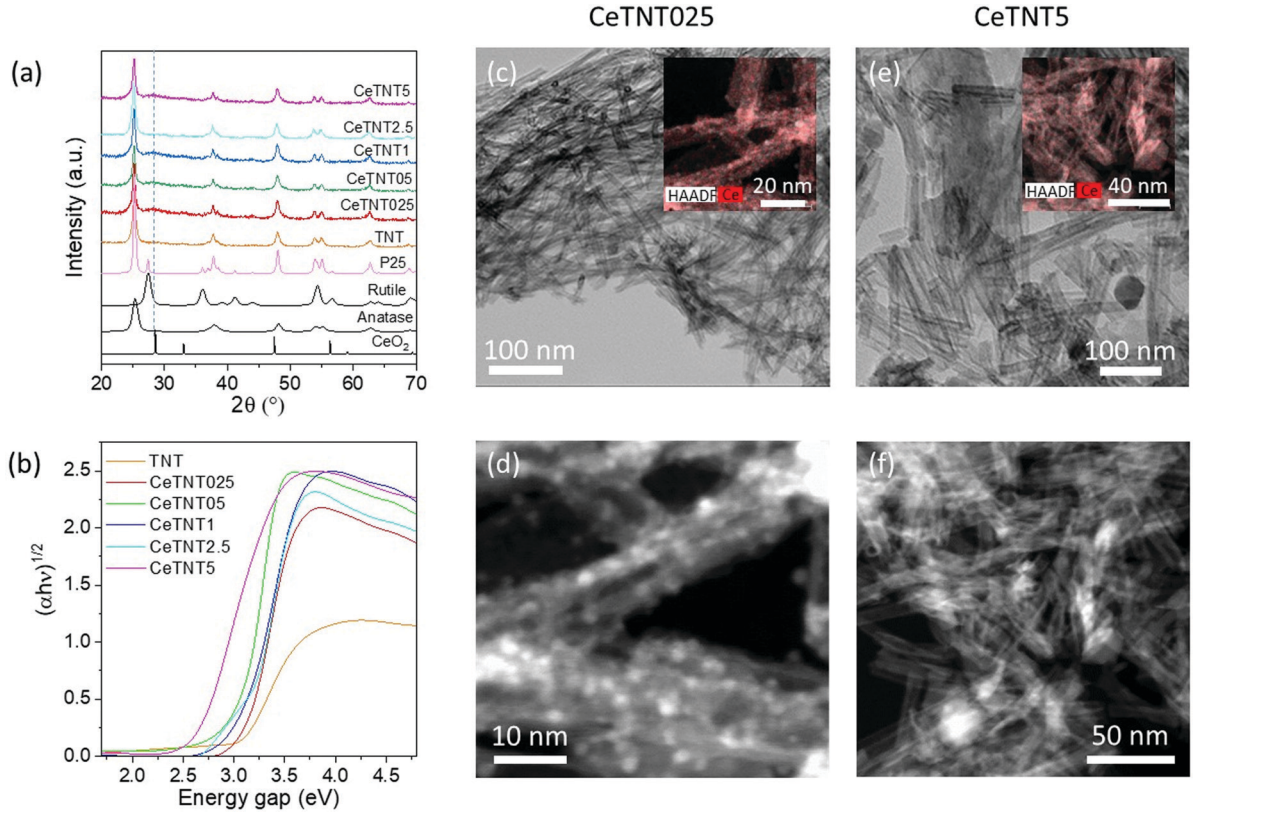

Fig. 1 Undoped and Ce-doped TNT series. (a) XRD patterns, including benchmarking anatase, rutile and P25. (b) $(\alpha h\nu)^{1/2}$ *vs.* photoenergy (eV) plot. TEM/HAADF images for samples CeTNT025 (c and d) and CeTNT5 (e and f). The insets in (c) and (e) show the EDS maps for Ce overlapping the STEM images.

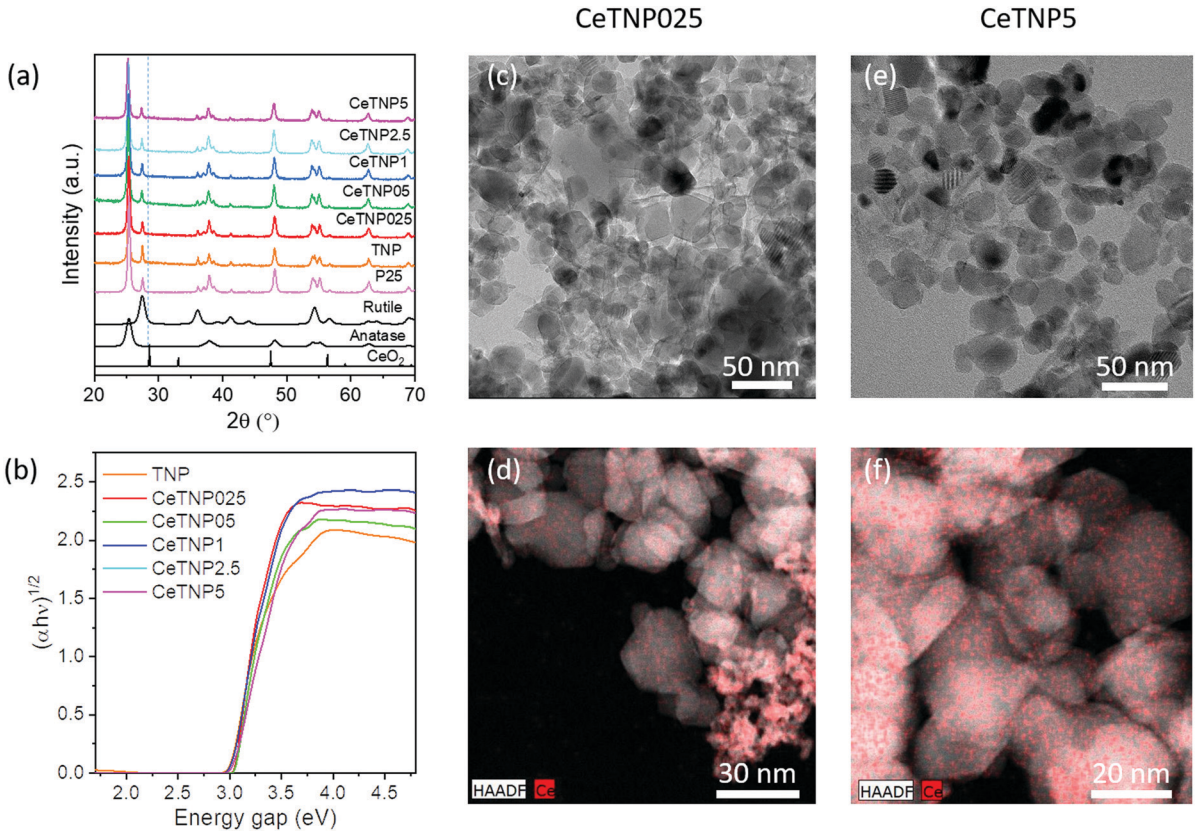

Fig. 2 Undoped and Ce-doped TNP series. (a) XRD patterns, including benchmarking anatase, rutile and P25. (b) $(\alpha h\nu)^{1/2}$ *vs.* photoenergy (eV) plot. TEM/HAADF images for samples CeTNP025 (c and d) and CeTNP5 (e and f). (d) and (f) show the EDS maps for Ce overlapping the STEM images.

The porous nature of the prepared materials was evaluated by N_2 physisorption at −196 °C and the textural properties (specific surface area, S_{BET}, and total pore volume, V_p) are summarized in Table 1. In order to compare the samples with a titania benchmark, Degussa P25 was also analyzed. The synthesized nanostructures, both nanoparticles and nanotubes, present type IV isotherms with H3 hysteresis loops (not shown), characteristic of mesoporous materials. While the CeTNT*x* series shows quite a low specific surface area, ranging between 20 and 27 $m^2\ g^{-1}$, the CeTNP*x* series displays higher S_{BET} values, much higher than that of commercial P25 titania (55 $m^2\ g^{-1}$). Pure titania nanoparticles, TNP, show a BET specific surface area of 118 $m^2\ g^{-1}$, with a cumulative pore volume of 0.55 $cm^3\ g^{-1}$. Mixed oxide nanoparticles, CeTNP*x*, display

Table 1 Textural, structural, and optical parameters and kinetic constants of MB degradation in aqueous solution under UV and simulated solar light irradiation for pure titania samples (TNT and TNP) and ceria-titania systems (CeTNT*x* and CeTNP*x* series)

				TiO_2 phases[c] (wt%)				
Sample	CeO_2 loading (wt%)	S_{BET}[a] ($m^2\ g^{-1}$)	Pore volume[b] ($cm^3\ g^{-1}$)	X_A	X_R	E_g[d] (eV)	$K_{UV\ light}$[e] (min^{-1})	$K_{Solar\ light}$[e] (min^{-1})
TNT	—	27	0.13	100	—	3.20	0.011	0.010
CeTNT025	0.25	26	0.15	100	—	3.10	0.123	0.003
CeTNT05	0.5	26	0.16	100	—	3.05	0.036	0.004
CeTNT1	1.0	26	0.15	100	—	3.03	0.046	0.008
CeTNT2.5	2.5	21	0.14	100	—	2.90	0.055	0.019
CeTNT5	5.0	20	0.18	100	—	2.65	0.004	0.012
TNP	—	118	0.55	73	27	3.00	0.069	0.034
CeTNP025	0.25	99	0.45	79	21	3.00	0.146	0.029
CeTNP05	0.5	98	0.44	81	19	3.00	0.134	0.033
CeTNP1	1.0	92	0.41	81	19	2.95	0.105	0.039
CeTNP2.5	2.5	71	0.36	85	15	2.75	0.097	0.054
CeTNP5	5.0	65	0.35	79	21	2.75	0.056	0.052
P25	—	55	0.06	83	17	3.15	0.079	0.014

[a] N_2 physisorption data calculated with the BET method by N_2 physisorption at −196 °C. [b] Cumulative pore volume calculated at relative pressure $P/P_0 = 0.98$ by N_2 physisorption at −196 °C. [c] TiO_2 crystalline phases determined with the X'Pert High Score Program. [d] Band gap determined by DRUV-Vis spectroscopy. [e] Kinetic constants under UV and solar light irradiation, respectively.

textural properties very close to each other, with relatively lower BET values, ranging between 65 and 99 $m^2\ g^{-1}$ and a slight decrease of the total pore volume in the range 0.35–0.45 $cm^3\ g^{-1}$ (Table 1), indicating that although some CeO_2 species are blocking titania's pores, titania nanoparticles are not significantly affected by changes in the sample composition.

The surface atomic compositions of CeO_2–TiO_2 materials as well as the chemical states of the elements were estimated by X-ray photoelectron spectroscopy (XPS). O 1s, Ti 2p and Ce 3d core level spectra were recorded to determine the species present on the catalysts' surfaces. The binding energies of core level electrons for ceria-titania nanotube (CeTNT*x*) and nanoparticle (CeTNP*x*) systems are listed in Table S1 (ESI†).

The Ti 2p core level spectra for all the samples (Fig. 3a and b) showed asymmetric doublets at 463.4 eV and 583.3 eV, ascribed to the core levels of Ti $2p_{1/2}$ and Ti $2p_{3/2}$, respectively, characteristic of Ti^{4+} ions and very similar to that reported for pure TiO_2 nanosystems.[38] The peak separation Ti $2p_{1/2}$–Ti $2p_{3/2}$ was about 5.7 eV in all cases, indicating that Ti ions were present in the Ti^{4+} oxidation state coordinated octahedrally. By comparing both families of compounds, the Ti $2p_{3/2}$ BE values are slightly higher in the case of the TNT family where the titania polymorph phase present is anatase; instead, TNP samples possess both anatase and rutile polymorphs. The BE values were reported to be 458.4 eV for anatase[39] and 458.7 eV for rutile:[40] the expected tendency is just the opposite to that found experimentally, suggesting that the morphology of titania, rather than its crystalline phase, determines the lability of the electrons at the core level. After cerium ion incorporation, a slight shift of the signal towards lower binding energy was observed in the case of the CeTNT family. This effect is much more significant at higher Ce loadings, indicating a greater contribution of titanium in the lower oxidation state due to the interaction with Ce species on the catalysts' surfaces. However, the doublet separation (5.7 eV) indicates that titanium is in its (IV) oxidation state. The observed shift could be explained as due to the close interaction between ceria and titania species that eases oxygen mobility in the Ce–O–Ti system, leading to the formation of oxygen vacancies that are believed to be more reactive in redox processes,[41] thus improving the photocatalytic activity. The opposite tendency is obtained for the CeTNP family. A shift to higher BE values was reported to be due to ion incorporation in the substitutional site of the TiO_2 lattice or the formation of Ti–O–Me bonds, which in this case could be related to Ce insertion into the TiO_2 matrix as observed before in mixed Ce–Ti oxides containing different Ce and Ti loadings, where similar shifts in Ti signals happened.[42] Another possible reason for the peak shifts could be the existence of oxygen vacancies in the catalyst structure.[43]

The O 1s (Fig. 3c and d) core level signals of the CeTNT*x* family showed two contributions, and the O 1s peaks were located at 530.1 and 531.6 eV. The first one was due to the lattice oxygen of TiO_2 (BE related to CeO_2 (529.1 eV)) and the second one was due to the presence to surface oxygen: (O–, OH–, CO_3^{2-}, $-CO_2^{2-}$).[44] Upon incorporating ceria, as in the case of the Ti 2p signals, a shift to lower BE values was observed, indicating

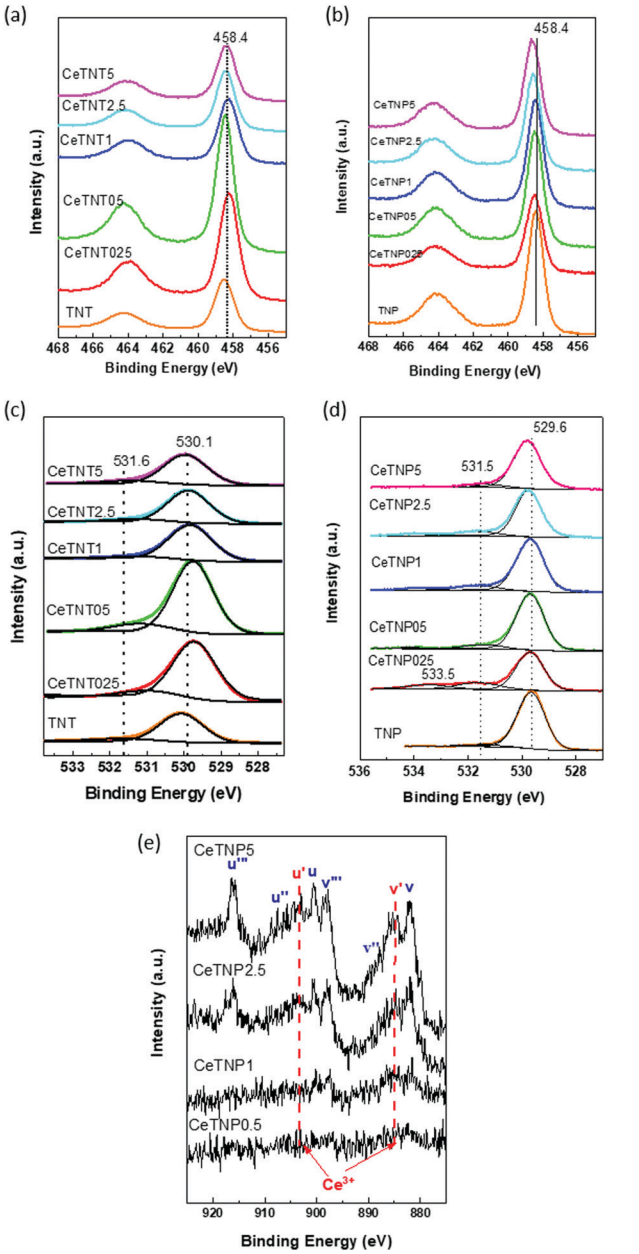

Fig. 3 XPS core level spectra: (a and b) Ti 2p signals of CeTNT*x* and CeTNP, respectively; (c and d) O 1s signals of CeTNT*x* and CeTNP, respectively; and (e) Ce 3d spectra of CeTNP samples.

an increase in the oxygen mobility.[43] In the case of the CeTNP*x* family, the O 1s main signal was located at a lower BE value compared to the CeTNT*x* family, 529.6 eV. Bare TNP also showed a contribution at 531.6 eV, characteristic of surface oxygen. Ce incorporation shifted the main signal to slightly higher values (Table S1, ESI†), suggesting that, taking into account the decrease in electronic density due to the Ce presence, the formation of a CeTiO mixed solution cannot be discarded. The most striking results come from the appearance of a third contribution after Ce incorporation into pure TNP.

This contribution appears at *ca.* 533.5 eV, which is reported in the literature to be due to chemisorbed oxygen.[45]

Ce 3d signals from the CeTNT*x* series were not detected, attributed to the low Ce quantity and probably its low dispersion. Nonetheless, Ce core-level photoelectron spectra were observed for CeTNP*x* samples and presented in Fig. 3e. The spectra were very noisy and the different contributions were only noticeable for Ce loadings greater than 0.5%. Thus, four spin–orbit doublets were present and indicated as $\nu(n)$ and $u(n)$: three due to Ce^{4+} species (ν (~882.2 eV) and u (~900.7 eV); ν'' (~888.8 eV) and u'' (~907.2 eV); ν''' (~898.2 eV) and u''' (~916.5 eV)) and one due to Ce^{3+} ones (ν' (~884.5) and u' (~903.3 eV)).[46] The presence of Ce^{4+} was dominant, although a great proportion of Ce^{3+} can be observed for samples containing 2.5 and 5% of Ce.

The HR-TEM micrographs in Fig. 1c–f show that the CeTNT*x* series presents randomly distributed titania nanotubes as the main structure, with nanometric ceria particles hosted inside titania nanotubes as demonstrated in the HAADF images. In the case of CeTNT5, although the majority of titania is in the form of nanotubes, the presence of some nanosphere structures can also be noticed in Fig. S2 (ESI†), suggesting an incomplete transformation of the nanopowder, from the sol–gel process (first step of synthesis) to the reaction with a basic solution at autogenous pressure (second step).[47] The analysis of nanotube and nanoparticle sizes was performed with ImageJ software. On the one hand, it revealed that CeTNT2.5 nanotubes presented a uniform length of approximately 122 nm and diameter of 6 nm, whereas those in samples with the highest Ce contents had an average length of 97 nm and diameter of 8 nm. On the other hand, it was found that Ce nanoparticles had a mean diameter of just 2 nm in samples with 2.5 wt% Ce and 1.6 nm in the CeTNT5 sample, which supports the fact that, as previously reported,[48] ceria nanoparticles grow inside titania nanotubes, ensuring a close contact between both phases and promoting the intermixing of ceria and titania oxides, which would favor the formation of Ce^{3+} cations. The small size of ceria particles may also explain the absence of reflections from ceria phases in XRD. For comparison purposes, HRTEM micrographs of pure titania samples, both TNP and TNT, are shown in Fig. S3 (ESI†).

EDX-STEM mapping was performed in order to study the dispersion of Ce on the catalysts, resulting in high dispersion of Ce nanoparticles in the titania nanostructures, as observed in the insets of Fig. 1c and e. EDX spectrum quantification (see Fig. S4, ESI†) showed that Ce nanoparticles had up to 3 wt% and 3.5 wt% Ce in the CeTNT2.5 and CeTNT5 systems, respectively, which are close to the theoretical values expected considering the local analyses carried out. The EDX spectrum also showed a contribution attributed to Na from the synthetic method employed.

Regarding the CeTNP*x* series, the HR-TEM micrographs in Fig. 2c–f and Fig. S5 (ESI†) revealed that titania nanoparticles were mainly square-shaped, with diameters between 20 and 25 nm, with the largest ones found in the samples with higher Ce contents. Although different cerium loadings seem not to be modify the general morphology of titania nanostructures, the EDX mapping in Fig. 2d showed that in the case of CeTNP2.5, despite the good dispersion of ceria, some agglomerates can also be observed, which are not present in the sample with 5 wt% Ce in Fig. 2f. As in the case of the CeTNT*x* series, the EDX spectrum quantification showed 3.85 wt% and 5 wt% Ce for CeTNP2.5 and CeTNP5, respectively, which are in good agreement with the theoretical values, suggesting a great dispersion of ceria in the titania matrix. The small NPs in Fig. 2d and Fig. S5 (ESI†) seem to be Ce-rich. Such a phenomenon is most likely due to the fact that Ce atoms tend to concentrate mainly at the surfaces of the titania structures. This is in agreement with the XRD and Raman results, in which no ceria phases are detected and (in XRD) no distortion of the crystal lattice is recorded, even at the highest Ce concentration. Since the small particles exhibit the highest specific surface area, it is reasonable that the Ce concentration is higher than that for large NPs.

The photo-responsive behavior of both nanostructured systems was explored by DRUV-Vis spectroscopy, to determine the energy gap, E_g. The DRUV-Vis spectra of the CeTNT*x* and CeTNP*x* series are shown in Fig. 1b and 2b, respectively, and the optical band gap values, estimated from the intercept of the extrapolated linear fit for the plotted experimental data of $(\alpha h\nu)^{1/2}$ (the exponent 1/2 was chosen for the indirect bandgap in titania) *versus* incident photon energy ($h\nu$) near the absorption edge, are listed in Table 1. The intrinsic interband absorption of the pure titania sample (TNT) was observed at wavelengths shorter than 400 nm (in the UV region) with E_g of 3.20 eV. Conversely, the CeO_2 doped-TiO_2 nanotubes showed a red shift in absorbance, as highlighted in Fig. 2b. This narrower band edge has been speculated to arise from the formation of Ce^{3+} ions that can induce some localized mid-gap states in the band gap.[49,50]

By increasing the loading of ceria into the titania matrix for the TNT series, a significant decrease of the band gap was in fact obtained. The E_g values of samples containing a low amount of ceria, CeTNT025, CeTNT05 and CeTNT1, are slightly lower, in the 3.10–3.03 eV range. CeTNT2.5 and CeTNT5 samples (containing 2.5 and 5.0 wt% ceria, respectively) display E_g values of 2.90 and 2.65 eV, respectively, much lower than that of the pure titania sample. The doping of titania with Ce ions produced a red shift in the absorption edges, increasing the available spectral region that could be used in photocatalytic processes, allowing harvesting visible light and generating a greater number of electrons and holes under visible-light irradiation that could actively participate in oxidation and reduction reactions. A significant decrease of the band gap upon increasing the Ce loading, even though less marked than that in the CeTNT family, was also obtained in the CeTNP*x* series (Fig. 2b), passing from 3.00 eV for the pure titania, TNP, to 2.75 eV for the 5.0 wt% ceria-doped sample, CeTNT5.

Photodegradation of methylene blue under UV and simulated solar light irradiation

Methylene blue, a heterocyclic aromatic compound, was taken as the photocatalytic probe molecule in this work since it is used as a textile, leather and paper dye that contributes to water pollution. It is well known that the amount of organic molecule adsorbed on the catalyst surface is affected by the pH value of

the solution and depends on both the specific surface area and the point of zero charge (PZC) of the material. Ceria typically shows a PZC around pH 7.2,[51] while that of titania is around 6.0–6.5.[52] The adsorption of MB *via* coulombic attraction is likely to be negligible at solution pH values below the PZC of the semiconductor, but increasingly significant at pH above the PZC value with an electrostatic absorption between the cationic dye[26] and the negatively charged surfaces of CeO_2 or TiO_2.[43–45] A value of pH around 5.5 is generally recommended for the degradation of methylene blue in an aqueous medium.[53]

The pathway for MB degradation under UV light irradiation on TiO_2-based materials is well known, based on the conversion of the organic dye into harmless CO_2, nitrate, ammonium, and sulfate ions, and it has been deeply investigated through LC/MS and GC/MS analyses of the intermediate compounds.[54] In this work, UV-visible spectra were recorded and monitored in the range 300–900 nm at different photoreaction times (after 5, 10, 15, 20, 40, 60, 90 and 120 min), also investigating the potential presence of leuco methylene blue (LMB) in solution. It is in fact known that MB can be reduced to colorless LMB, stable in a vacuum or under an inert atmosphere, which can be rapidly reduced back to MB[55] and both methylene blue and its reduced form exhibit their characteristic and strong absorbance bands in the 250–800 nm range. At the pH used to perform the catalytic test, no color change of the MB solution was noticed, which was also confirmed by the absorption profile of the dye in the visible region. This marks the stability of the MB solution in an acidic pH range as no absorption peak appeared around 520 nm,[55] the characteristic wavelength of the LMB peak.

Fig. 4a and b shows the MB UV-vis absorption spectra in dark mode and under UV light for the two nanostructures with the highest CeO_2 loading (5 wt%), taken as examples. The decrease in absorption at 664 nm has been ascribed to the degradation of benzene rings and heteropoly-aromatic linkages.[54] Since no other absorption bands were detected, it can be stated that the LMB form was not present in the reaction environment neither for nanotube samples nor for nanoparticle ones and that the sample solution bleaching was completely due to dye degradation. Fig. 4c–f presents the photocatalytic performance of the nanotube and nanoparticle series in the methylene blue decomposition in aqueous solution under UV and simulated solar light irradiation, while the corresponding pseudo-first order kinetic constant values, k, calculated using the data from the non-stationary regime during the light phase, are listed in Table 1. A comparison with commercial P25 Degussa TiO_2, usually employed as a standard benchmark photocatalyst, was also made since it shows high activity in the investigated reaction.

Fig. 4c and e presents the photocatalytic activity of the CeTNT*x* series in the monitored period of 120 minutes. After 30 min of equilibration in the dark (switching off light), a certain amount of MB is adsorbed on the surfaces of the samples, with a 35%–45% decrease in dye concentration in the solution when increasing the CeO_2 loading from 0.25 up to 5.0 wt%.

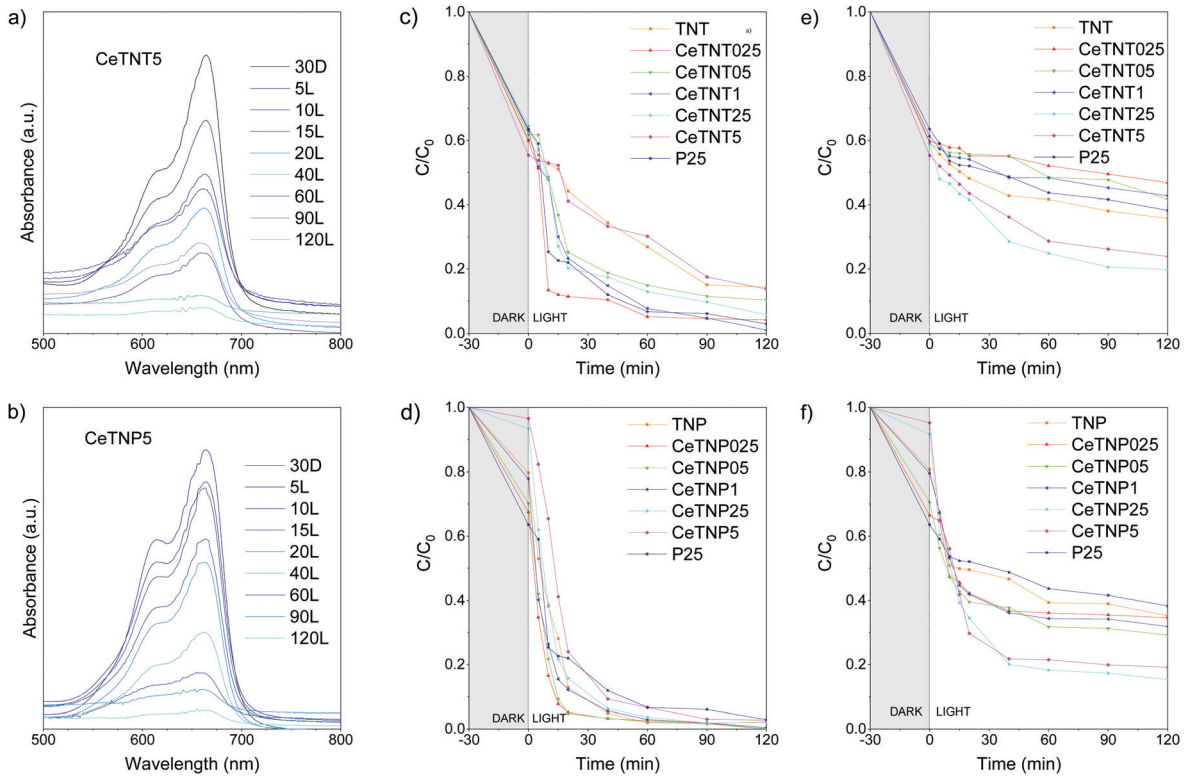

Fig. 4 (a and b) UV-Visible spectra recorded at different times, from 30 min under dark conditions (30D) to 120 min under UV light irradiation (120L), for the two 5.0 wt% CeO_2–TiO_2 nanostructures: (a) CeTNT5 sample and (b) CeTNP5 sample. (c–f) MB photodegradation test in aqueous solution: CeTNT*x* (c) under UV light irradiation and (e) under simulated solar light; and $CeTNP_x$ (d) under UV light irradiation and (f) under simulated solar light.

Under UV light, all the CeTNT*x* photocatalysts show a very interesting catalytic performance, except for the CeTNT5 sample, with the CeTNT025 (0.25 wt% ceria-containing nanosystem) being the most photoactive one, with a kinetic constant for MB degradation of 0.123 min^{-1}, and able to photodegrade almost completely (99%) the dye after 120 minutes. As to the pure titania sample, TNT, its performance is lower than that of the P25 benchmark, which could be ascribed to the lower surface area of TNT in comparison with commercial titania (27 m^2 g^{-1} and 55 m^2 g^{-1}, respectively). Regarding the Ce-containing samples, the presence of ceria seems to improve the photocatalytic activity with respect to pure nanotubes at low loadings, while the catalytic performance worsens for a 5 wt% ceria loading. As suggested by the TEM and EDX measurements, the relatively high coverage of the surface by ceria nanoparticles could be hindering pollutant molecules' access to TiO_2 active sites, thus lowering their photocatalytic activity.

These materials were also tested under the same operating conditions under standard simulated solar light irradiation. The CeTNT2.5 sample displayed the highest reaction rate (k = 0.019 min^{-1}), as well as the best performance, in comparison with the other Ce-containing nanotubes and the pure titania samples (TNT and P25). The catalytic behaviour of these systems is in accordance with the E_g values obtained (Table 1): the lower the band gap of the sample, the higher its activity under simulated sunlight. Although also the sample containing 5 wt% ceria displayed a band gap (2.65 eV) suitable to harvest the visible portion of the solar spectrum, its catalytic activity is quite lower in comparison to the sample containing 2.5 wt% ceria, probably due to the weak interaction between TiO_2, the most photoactive phase, and CeO_2 in this sample as a consequence of the high loading of Ce covering the photocatalyst's surface, as confirmed by the HRTEM. As expected, both pure TiO_2 samples, the freshly synthesized TNT and commercial P25 chosen for comparison purposes, showed kinetic constants higher under UV than solar light irradiation, due to their wide energy gap values (3.20 and 3.15 eV, respectively). As for the CeTNP*x* series (Fig. 4d–f), under UV light irradiation all the samples displayed high activity towards the desired reaction, achieving an almost complete dye photodegradation in the monitored time. In particular, the results suggest that the presence of small amounts ($<$2.5 wt%, the best performance for 0.25 wt%) of ceria in this kind of nanostructure is highly beneficial for the kinetics of the reaction.

The highest k constant under UV light (0.146 min^{-1}) was obtained for the CeTNP025 sample, able to reach a residual C/C_0 value of 5% just after 20 min and photodegrade completely MB after 2 h. Under simulated sunlight irradiation, the catalytic behavior of the nanoparticle-based series shows the same trend of the CeTNT*x* series, following the increasing amount of ceria in the titania matrix and, as expected, the decreasing band gap values. Samples with 2.5 and 5.0 wt% ceria exhibit a much higher activity in degrading the organic dye under solar light with respect to their congeners, with k values of 0.054 and 0.052 min^{-1}, respectively. Charge dynamics in the two series of samples was investigated through time-resolved photoluminescence (TRPL), by monitoring the modification of the PL decay spectra upon MB addition in suspensions containing CeTNT*x* and CeTNP*x*. Similar analysis was already proposed for other luminophores to investigate the PL quenching properties of electron scavengers during photocatalytic processes.[56] The emission and excitation wavelengths were selected as: λ_{em} = 400 nm and λ_{ex} = 250 nm ($\sim$4.96 eV) aiming at studying the evolution of the 4f–5d transition of Ce^{3+}.[57] The PL emission at 400 nm was also observed in the as-prepared TiO_2 (TNP) sample, which is similar to the PL of ultrafine TiO_2 powder reported by S. Kaniyanka and co-workers.[58] The presence of MB in solution, as already highlighted by the photocatalytic measurements in both the series of samples, induces a fast charge transfer from the photoexcited electrons in the conduction band of the mixed oxide to the lowest unoccupied molecular orbital (LUMO) of MB. Such a recombination path competes with the radiative recombination originating the PL under investigation, affecting its time decay behavior.

In Fig. 5 the time resolved PL at 400 nm emission wavelength is reported for a series of selected samples in solution with and without MB from both the series. In all the samples, the TRPL intensity curve is characterized by the presence of two time constant decays, the first one with the characteristic decay time in the range of few ns (falling into the limit of the instrument), and the second one in the order of around 110 μs. The presence of MB modifies the TRPL spectra. The relative intensity of fast decay increases, while that of slow decay decreases. However, the long decay constant of around 110 μs remains the same in both Ce-TNT (TNP) and Ce-TNT (TNP)/MB, which is in agreement with the hypothesis that the MB acts as a carrier scavenger to Ce-TiO_2. This also indicates that uptake (and degradation) of MB did not introduce any new excited state around 400 nm. Among all five measured samples as shown in Fig. 5, the Ce-TNT25 sample presents the most significant drop in the intensity of the slow decay component after mixing with MB, which can be correlated and is in agreement with the results on MB degradation presented in Fig. 6.

Since the recyclability of a catalyst is very important for its practical use, a stability and reusability test of the best performing photocatalysts under UV light irradiation, CeTNT025 and CeTNP025 (both containing 0.25 wt% CeO_2 in TiO_2), was carried out using the same operating conditions as before. As shown in Fig. 6, a slight decrease in the activity of the catalyst during repeated cycles was observed. Adsorption of MB (initial dark period) was slightly reduced, probably due to the partial blockage of the active sites by the degradation products. However, after three recycling processes, both the Ce-doped nanotubes and nanoparticles were still active in the MB dye degradation under UV light, with a slightly lower efficiency, suggesting a very good physico-chemical stability of these samples.

The best performing samples were recovered after a 3-cycle reusability test, washed, dried at 110 °C in air flow and then analyzed by X-ray diffraction. As expected, in both the diffractograms (Fig. S6, ESI†) the size of titania crystallites did

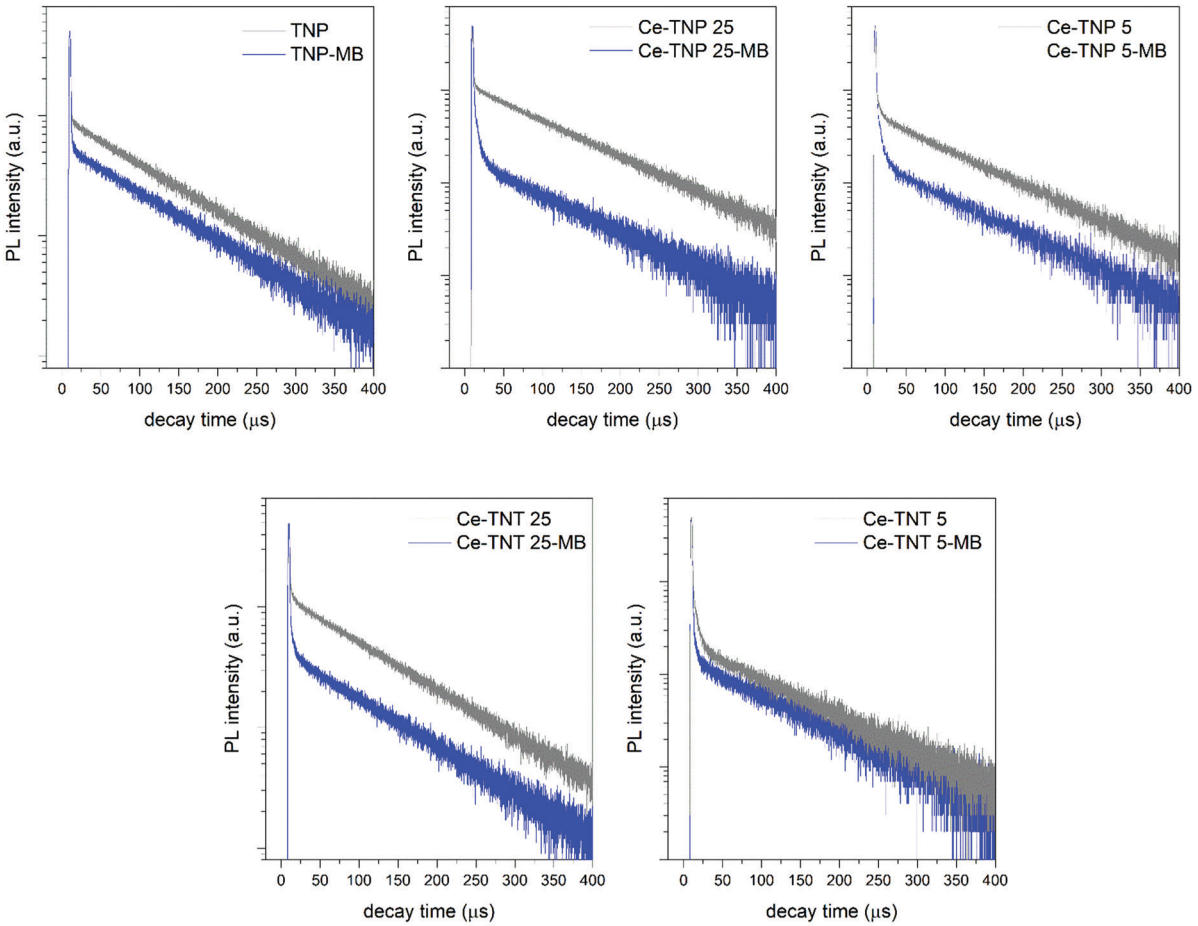

Fig. 5 TRPL decay spectra for selected samples of the two TNP and TNT series. λ_{ex} = 250 nm; λ_{em} = 400 nm.

not change, and no new peaks related to cerium- or titanium-based phases were detected after the reaction.

The used CeTNT025 and CeTNP025 systems were also analyzed by N_2 physisorption at −196 °C. The BET specific surface areas of the samples slightly decreased after the recyclability test, passing from 26 to 22 $m^2\ g^{-1}$ for CeTNT025 and from 99 to 91 $m^2\ g^{-1}$ for CeTNP025, attributed to the partial pore blocking by the degradation by-products. Regarding the catalytic activity, a slight decrease of MB absorption in the initial dark period can be noticed by comparing the profiles of the first and third cycles, for both nanoparticles and nanotubes (Fig. 6a and b), most probably due to the above mentioned surface area decrease.

From the obtained results, it could be assumed that the formation of a ceria–titania composite can lead to the formation of a heterojunction structure, with synergistic effects for harvesting visible light, and beneficial to the separation and transfer of photogenerated charge carriers.

Moreover, a very small amount of ceria, 0.25 wt%, has been found to be optimal to cover enough TiO_2 surface with ceria ions and leaving enough uncovered titania surface where the organic pigment can get adsorbed and degraded under UV light. Such a loading can allow ceria to produce electrons that are immediately transferred to titania and this can lead to an efficient separation of electrons and holes across the boundary between TiO_2 and CeO_2 and thus reduce the recombination processes. A ceria loading in the range 0.5–2.5 wt% has led to higher activity under UV light than that obtained by pure titania, while a ceria loading of 5 wt% seems to have detrimental effects on the photocatalytic activity with respect to the bare titania matrix.

Conversely, under sunlight irradiation the doping of titania with Ce ions seems to have produced a red shift in the absorption edges (Table 1), increasing the available spectral region that could be used in photocatalytic processes, allowing harvesting visible light and generating a greater number of electron and hole pairs under this less energetic radiation. From the experimental results, it seems that a ceria amount of about 2.5 wt% is the optimum for enhancing the photocatalytic performance of a TiO_2 matrix.

Besides the doping with ceria, the morphologies of the titania-based nanostructures also seem to have a significant effect on their photo-activity. The CeTNP*x* series showed a lower dye adsorption after 30 min of equilibration in the dark, and higher MB photodegradation activity and *k* values, both under UV and simulated sunlight irradiation, with respect to

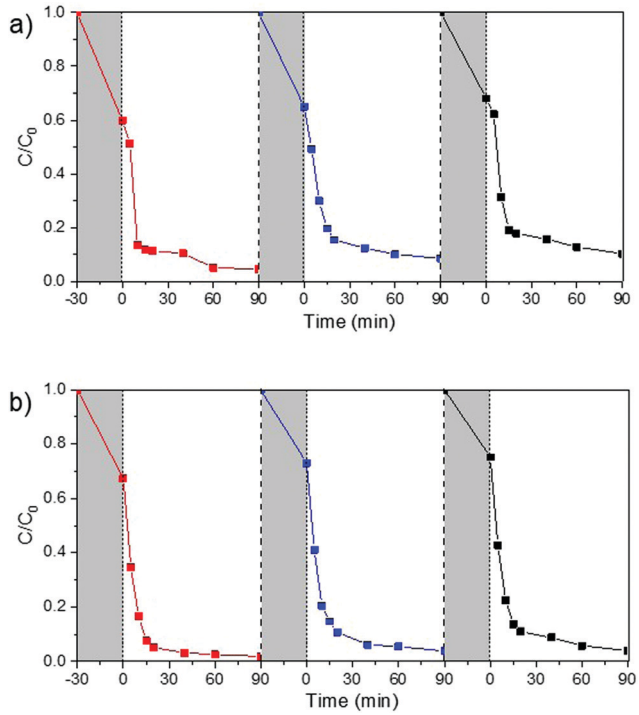

Fig. 6 MB photodegradation recycling performance of (a) CeTNT025 and (b) CeTNP025 catalysts under UV light irradiation.

the CeTNT*x* series. As previously reported, this suggests that less ordered nanostructures, like nanoparticles, are more photoactive than nanotubes or nanosheets in dye photodegradation (see Table 2). Under similar reaction conditions (but with lower performances, see Table 2), Bonfanti-Vieira *et al.*[59] reported that Ce-doped titania with combined morphologies such as nanotubes, nanosheets and nanoparticles achieved almost a complete degradation of both MB and polyvinylpyrrolidone (PVP) pollutants, over 90% both under UV and simulated solar light irradiation. In this work it was also suggested that it is in fact ceria addition that induces the disorder in the nanostructures. It is not only the less ordered structure morphology that enhances the catalytic activity, but also the surface area to volume ratio of the nanostructures. Three-dimensional nano-architectures with large surface area to volume ratios and high light absorbance have recently emerged as particularly promising candidates for the degradation of organic pollutants.

Li *et al.*[60] studied the degradation of ciprofloxacin pollutant under UV-Vis irradiation using eco-friendly produced TiO_2 with two different morphologies, rod-like and tripyramid-like, demonstrating that the three dimensional architecture achieved 90% degradation after 60 minutes of reaction, while rod-like one attained just 50% of degradation, which could be attributed to the improved surface area due to the special tri-dimensional structures. Likewise, Bergamonti *et al.*[61] investigated the photocatalytic performance of TiO_2-supported chitosan scaffolds in amoxicillin photodegradation under UV-Vis irradiation, with total degradation even with large quantities of pollutant. The advantage in the use of these scaffold titania structures lies in the possibility of modulating their shape and size, which provides a high surface area to volume ratio, as well as improving the stability and handling of the titania photocatalyst.

This could also be ascribed to the higher specific surface area that allows a better dispersion of ceria on the catalyst surface and a higher interaction between the dye and the active sites of the inorganic matrix.

Experimental

Synthesis of TiO_2 nanotubes

TiO_2 nanotubes were prepared by a two-step hydrothermal route, where titania nanopowder was first obtained by a sol–gel process, and then nanotubes were prepared by a dehydration reaction using TiO_2 nanopowder as the starting material. In the sol–gel process, 5 mL of titanium tetraisopropoxide (TTIP) (Sigma-Aldrich, 97%) were added to 15 mL of 2-propanol (Sigma-Aldrich, 99.5%) and 250 mL of MilliQ water into a flask under vigorous stirring and aged at 70 °C for 10 h. Then the pH of the reaction mixture was set at 2 by adding 0.6 M hydrochloric acid (Sigma-Aldrich, 37%).

The product was separated by centrifugation, washed with absolute ethanol (Sigma-Aldrich, >99%) and dried at 80 °C overnight. 0.5 g of product was then dissolved in 30 mL of 10 M NaOH (VWR Chemicals) aqueous solution, placed in a Teflon autoclave and kept at 130 °C and autogenous pressure for 24 h. The obtained product was recovered by centrifugation, and filtered and washed with MilliQ water, 0.1 M HNO_3 (VWR Chemicals, ≥90.0%) aqueous solution and finally hot MilliQ water until neutral pH was achieved.

Table 2 Photocatalytic degradation of MB dye in aqueous solution under UV or solar light irradiation

Photocatalyst	Dopant loading (wt%)	Dye concentration (mg L^{-1})	Catalyst loading (g L^{-1})	Irradiation source	Irradiation time (min)	Dye degradation (%)	k (min^{-1})	Ref.
TiO_2–CeO_2 nanosheets	1.56	10	1	λ > 420 nm	180	70	0.0073	62
CeO_2/TiO_2 nanotubes	15	15	0.8	λ > 400 nm	150	>99	0.032	63
WO3/TiO_2	10	10	0.6	UV	180	98.92	0.017	64
ZnS/TiO_2	0.2	20	0.5	UV-Vis	120	100	—	65
Gd–Si–TiO_2	0.66–0.06	10	0.3	Solar light	120	100	—	66
Ce–TiO_2	0.85	20	0.5	Visible	160	90	0.021	59
TiO_2-CeO_2 nanoparticles (CeTNP025)	0.25	19.2	0.68	UV	120	99	0.146	This work
				Solar light	120	60	0.029	This work

The sample was dried at 80 °C overnight and annealed at 400 °C for 2 h (heating rate 1 °C min^{-1}) in air flow to obtain titania nanotubes. The sample was identified as TNT, where T = titania and NT = NanoTubes.

Synthesis of TiO_2 nanoparticles

Titania nanoparticles were prepared by a hydrothermal reaction following a procedure reported in the literature[67] with some modifications. 1.0 g of titanium dioxide P25 (Aeroxide Evonik Industries) was dispersed in 80 mL of a 10 M KOH (VWR Chemicals) aqueous solution under vigorous stirring for 1 h. Then the suspension was transferred into a Teflon-lined autoclave and heated at 160 °C for 6 h. The product was separated by centrifugation and washed with MilliQ water, 0.1 M HNO_3 aqueous solution and hot MilliQ water until neutral pH was achieved. The product was dried at 80 °C for 48 h and then thermally treated at 400 °C for 2 h (heating rate 1 °C min^{-1}) in air flow to obtain titania nanoparticles. The sample was identified as TNP, where T = titania and NP = NanoParticles.

Synthesis of CeO_2–TiO_2 photocatalysts

Ceria-containing nanotubes and nanoparticles were prepared by following the procedures reported in Sections 2.1 and 2.2, respectively, adding the required amount of $Ce(NO_3)_3{\cdot}6H_2O$ (Sigma-Aldrich) to a solution of TTIP, 2-propanol and MilliQ water and to an aqueous solution of KOH to obtain ceria-titania nanotubes (CeTNT*x* series) and ceria-titania nanoparticles (CeTNP*x* series), respectively.

The samples were referred to by the acronyms CeTNT*x* and CeTNP*x*, where Ce = ceria, T = titania, NT = NanoTubes, NP = NanoParticles and x = 0.25, 0.5, 1.0, 2.5, and 5.0 wt% CeO_2.

Characterization of catalysts

X-ray powder diffraction (XRPD) patterns were collected on a Philips PW 1319 diffractometer with a voltage of 40 kV and a Bragg–Brentano reflection configuration and a Cu anode ($K\alpha_1$ = 1.5406 Å). The measures were recorded in the range from 10° to 80° of 2θ, with a step size of 0.05° (2θ).

N_2 physisorption measurements were performed at −196 °C with ASAP 2010 apparatus of Micromeritics. After outgassing at 130 °C for 12 h at 0.67 Pa, the N_2 isotherms were acquired to determine the specific surface areas through the BET equation (S_{BET}), the specific pore volume (V_s) calculated at P/P_0 = 0.98, and the pore size distribution by the BJH (Barrett–Joyner–Halenda) method, taking the data of the desorption branch and assuming a cylindrical pore model.

Raman spectra were recorded using a WiTec CRM-200 microRaman system equipped with an Olympus LMPlanFL 20×/0.40 objective. The excitation laser wavelength is 633 nm and the laser power on the samples was kept at 1 mW.

UV-vis diffuse reflectance (DRUV-vis) spectra were collected with a Perkin Lambda 35 UV-vis spectrophotometer, equipped with integrating sphere accessories, for wavelengths ranging from 300 to 800 nm. The absorption coefficient (α) was calculated as follows: $\alpha = \ln(1/T)/d$, where T is the measured transmittance and d is the optical path length. The band gap energy, E_g, was determined through the α value (m^{-1}) from a plot of $(\alpha h\nu)^{1/n}$ *versus* photon energy ($h\nu$), where h is Planck's constant, ν is the frequency (s^{-1}) and the exponent n is the power factor of the optical transition mode, depending on the nature of the electronic transitions responsible for the absorption and which is equal to 2 for allowed indirect transitions. The intercept of the tangent to the absorption curves was used to estimate the band gap (E_g) values.

Time resolved PL was recorded using an FLS980 photoluminescence spectrometer from Edinburgh Instruments, which is equipped with a high-speed photomultiplier tube. The samples were excited with 250 nm UV light from a microsecond Xe flashlamp and the decay spectra of sample emission at 400 nm were collected in CeTNT*x*–water dispersion both before and after mixing with MB.

High resolution transmission electron microscopy (HR-TEM) was performed by using a TALOS F200x instrument. TEM analysis was performed at 200 kV and 5.5 μA and scanning transmission electron microscopy (STEM) with a HAADF detector was carried out at 200 kV and 200 pA. ImageJ software (ImageJ 1.51K) was used to estimate the average particle size distribution.

X-ray photoelectron spectra (XPS) were collected using a Physical Electronics PHI 5700 spectrometer with non-monochromatic Mg Kα radiation (300 W, 15 kV, 1253.6 eV) for the analysis of the core level signals of C 1s, O 1s, Ti 2p, and Ce 3d, and with a multichannel detector. The binding energy (BE) values were referenced to the C 1s peak (284.8 eV) from the adventitious contamination layer. The spectrometer energy scale was calibrated using Cu $2p_{3/2}$, Ag $3d_{5/2}$, and Au $4f_{7/2}$ photoelectron lines at 932.7, 368.3, and 84.0 eV, respectively. The PHI ACCESS ESCA-V6.0 F software package and Multipak v8.2b were used for acquisition and data analysis, respectively. A Shirley-type background was subtracted from the signals. Recorded spectra were always fitted using Gauss–Lorentz curves, in order to determine the binding energies of the different element core levels more accurately. The error in BE was estimated to be *ca.* 0.1 eV.

Photocatalytic activity

The degradation of methylene blue, MB, was chosen as a test reaction to evaluate the photocatalytic activity of the synthesized materials both under UV and simulated solar light irradiation. A 300 mL Pyrex photochemical reactor was used, with an initial concentration of the target molecule of 6.0×10^{-5} M at pH = 5.0. All the degradation experiments were carried out at 20 °C. The amount of photocatalyst was fixed at 0.68 g L^{-1}. Under UV light, a 125 W high pressure mercury lamp, operating at wavelengths between 180 and 420 nm with a peak at 366 nm, was used. When samples were tested under simulated solar light irradiation, a Sunlight Solar Simulator with an AM1.5G filter and a 100 Watt xenon arc lamp (Abet Technologies) was used. Before the catalytic measurements under simulated sunlight, a reference cell was used to set the intensity of the light source to standard illumination conditions. The photon flux was measured by using a Delta

OHM radiometer HD2302.0 leaned against the external wall of the photoreactor containing only pure water. To reach the adsorption equilibrium before irradiation, the suspension was stirred in the dark for 30 min. After switching on the lamp, aliquots of 2 mL of the aqueous suspension were collected from the reactor and filtered through a 0.45 μm PTFE Millipore disc to remove the catalyst powder.

A Shimadzu UV-2450 UV-Vis spectrometer was used for the determination of the dye concentration, after calibration. The degradation processes were monitored following the absorbance at the maximum (664 nm) of the UV-vis spectrum of the target molecule. Since the degradation pathway for the selected dye is known with high reliability,[54] the eventual formation of by-products was checked, monitoring the overall UV-vis spectrum of the solutions recovered at different times during the degradation experiments.

The rate constant was calculated according to (1):

$$\ln\frac{C}{C_0} = -kt \quad (1)$$

where C is the concentration after time t, C_0 represents the initial concentration and k is the pseudo-first order rate constant (min^{-1}), calculated as (2):

$$k = 2.303 \times \text{slope} \quad (2)$$

To evaluate the stability and reusability of the photocatalysts, a 3-cycle recycling test was performed. The powder sample was collected by centrifugation, washed with deionized water and dried overnight after each photocatalytic cycle for the recycling test.

Conclusions

In the present work, nanostructured TiO_2 samples with different CeO_2 loadings in the range 0.25–5.0 wt% were hydrothermally synthesized to obtain nanotubes (TNT series) and nanoparticles (TNP series). These two Ce-doped titania series were used as photocatalysts in the degradation of methylene blue in aqueous solution, under both UV and simulated solar light irradiation at room temperature and atmospheric pressure. It was demonstrated that their morphology plays a crucial role in their photocatalytic activity: the less ordered structures, the CeTNP series, displayed a greater catalytic performance, most probably due to the higher surface area to volume ratio and the better dispersion of ceria nanoparticles, together with their high specific surface area. The photoresponse confirmed that a suitable E_g, obtained by tuning the amount of ceria in the framework of titania and consequently lowering the band gap to harvest visible light, can enhance the catalytic activity. Ce-containing samples showed in fact a higher MB degradation rate than the corresponding pure titania nanosystems, under both simulated solar light and UV irradiation, which could be attributed to both the E_g decrease and oxygen vacancies supplied by Ce redox pairs. It was also observed that Ce acts like a promoter, as samples with high ceria contents showed worse conversions, probably due to several factors such as low specific surface area due to the pore blockage or hindering of active titania sites by ceria nanoparticles. In fact, the sample that showed the best catalytic performance was Ce-doped titania nanoparticles with 0.25 wt% Ce, which were able to degrade more than 90% of MB in less than 20 minutes of reaction and exhibited great stability after 3 reutilisation cycles. These results pave the way for the development of highly efficient titania-based photocatalysts with low dopant concentration, whose structural, optical and electronic properties can be controlled through dopant concentration and suitable preparation conditions.

Author contributions

C. A., I. B.-M., A. I.-M., S. Y., A. T., H. Z.: investigation and formal analysis. E. R.-C., A. V., A. I.-M., E. M.: conceptualization, funding acquisition, and providing resources. E. M., A. V., and A. I.-M.: supervising and writing the original draft. All the authors reviewed and approved the manuscript.

Conflicts of interest

There are no conflicts to declare.

Acknowledgements

The authors would like to acknowledge the project RTI2018-099668-BC22 of Ministry of Science, Innovation and Universities and FEDER funds, for financial support. A. I. M. thanks the Ministry of Economy and Competitiveness for a Ramón y Cajal contract (RyC-2015-17870). A. V. and S. Y. acknowledge the Kempe Foundation, the Knut & Alice Wallenberg Foundation and the ÅForsk Foundation for financial support.

Notes and references

1 M. A. Hassaan and A. El Nemr, Health and Environmental Impacts of Dyes: Mini Review, *Am. J. Environ. Sci. Eng.*, 2017, **1**, 64–67.
2 E. Lacasa, P. Cañizares, F. C. Walsh, M. A. Rodrigo and C. Ponce-de-León, Removal of methylene blue from aqueous solutions using an Fe^{2+} catalyst and *in situ* H_2O_2 generated at gas diffusion cathodes, *Electrochim. Acta*, 2019, **308**, 45–53.
3 T. H. Tu, P. T. N. Cam, L. V. T. Huy, M. T. Phong, H. M. Nam and N. H. Hieu, Synthesis and application of graphene oxide aerogel as an adsorbent for removal of dyes from water, *Mater. Lett.*, 2019, **238**, 134–137.
4 V. B. Yadav, R. Gadi and S. Kalra, Clay based nanocomposites for removal of heavy metals from water: A review, *J. Environ. Manage.*, 2019, **232**, 803–817.
5 Y. Deng and R. Zhao, Advanced Oxidation Processes (AOPs) in Wastewater Treatment, 2015.
6 M. Pelaez, N. T. Nolan, S. C. Pillai, M. K. Seery, P. Falaras, A. G. Kontos, P. S. M. Dunlop, J. W. J. Hamilton, J. A. Byrne, K. O'Shea, M. H. Entezari and D. D. Dionysiou, A review on

the visible light active titanium dioxide photocatalysts for environmental applications, *Appl. Catal., B*, 2012, **125**, 331–349.

7 M. R. Hoffmann, S. T. Martin, W. Choi, D. W. Bahnemann and D. W. Bahnemann, Environmental Applications of Semiconductor Photocatalysis, *Chem. Rev.*, 1995, **95**, 69–96.

8 Q. Zhang, J.-B. Joo, Z. Lu, M. Dahl, D. Q. L. Oliveira, M. Ye and Y. Yin, Self-Assembly and Photocatalysis of Mesoporous TiO_2 Nanocrystal Clusters, *Nano Res.*, 2011, **4**, 103–114.

9 L. E. Oi, M.-Y. Choo, H. V. Lee, H. C. Ong, S. B. A. Hamid and J. C. Juan, Recent advances of titanium dioxide (TiO_2) for green organic synthesis, *RSC Adv.*, 2016, **6**, 108741–108754.

10 I. Barroso-Martín, E. Moretti, A. Talon, L. Storaro, E. Rodríguez-Castellón and A. Infantes-Molina, Au and AuCu Nanoparticles Supported on SBA-15 Ordered Mesoporous Titania-Silica as Catalysts for Methylene Blue Photodegradation, *Materials*, 2018, **11**, 890–906.

11 Q.-E. Zhao, W. Wen, Y. Xia and J.-M. Wu, Titania nanowires growing from P25 nuclei: Facile synthesis and the improved photocatalytic activity, *J. Phys. Chem. Solids*, 2019, **124**, 192–198.

12 K. Nakata and A. Fujishima, TiO_2 photocatalysis: Design and applications, *J. Photochem. Photobiol., C*, 2012, **13**, 169–189.

13 X. Yu, Z. Zhao, J. Zhang, W. Guo, L. Li, H. Liu and Z. L. Wang, One-step synthesis of ultrathin nanobelts-assembled urchin-like anatase TiO_2 nanostructures for highly efficient photocatalysis, *CrystEngComm*, 2017, **19**, 129–136.

14 B. Ohtani, Photocatalysis A to Z—What we know and what we do not know in a scientific sense, *J. Photochem. Photobiol., C*, 2010, **11**, 157–178.

15 J. Ananpattarachai, P. Kajitvichyanukul and S. Seraphin, Visible light absorption ability and photocatalytic oxidation activity of various interstitial N-doped TiO_2 prepared from different nitrogen dopants, *J. Hazard. Mater.*, 2009, **168**, 253–261.

16 M. R. D. Khaki, M. S. Shafeeyan, A. A. A. Raman and W. M. A. W. Daud, Application of doped photocatalysts for organic pollutant degradation - A review, *J. Environ. Manage.*, 2017, **198**, 78–94.

17 F. Zhou, C. Yan, H. Wang, S. Zhou and S. Komarneni, Fabrication and characterization of TiO_2/Sepiolite nanocomposites doped with rare earth ions, *Mater. Lett.*, 2018, **228**, 100–103.

18 C. Belver, J. Bedia, M. A. Álvarez-Montero and J. J. Rodriguez, Solar photocatalytic purification of water with Ce-doped TiO_2/clay heterostructures, *Catal. Today*, 2016, **266**, 36–45.

19 M. Pedroni, F. Piccinelli, S. Polizzi, A. Speghini, M. Bettinelli and P. Haro-González, Upconverting Ho–Yb doped titanate nanotubes, *Mater. Lett.*, 2012, **80**, 81–83.

20 S. Rajendran, M. M. Khan, F. Gracia, J. Qin, V. K. Gupta and S. Arumainathan, Ce^{3+}-ion-induced visible-light photocatalytic degradation and electrochemical activity of ZnO/CeO_2 nanocomposite, *Sci. Rep.*, 2016, **6**, 1–11.

21 H. Abdullah, M. R. Khan, M. Pudukudy, Z. Yaakob and N. A. Ismail, CeO_2–TiO_2 as a visible light active catalyst for the photoreduction of CO_2 to methanol, *J. Rare Earths*, 2015, **33**, 1155–1161.

22 A. Infantes-Molina, A. Villanova, A. Talon, M. G. Kohan, A. Gradone, R. Mazzaro, V. Morandi, A. Vomiero and E. Moretti, Au-Decorated Ce-Ti Mixed Oxides for Efficient CO Preferential Photooxidation, *ACS Appl. Mater. Interfaces*, 2020, **12**, 38019–38030.

23 I. Barroso-Martín, C. Alberoni, E. Rodríguez-Castellón, A. Infantes-Molina and E. Moretti, Recent advances in photo-assisted preferential CO oxidation in H_2-rich stream, *Curr. Opin. Green Sustainable Chem.*, 2020, **21**, 9–15.

24 E. Moretti, L. Storaro, A. Talon and M. Lenarda, One-pot mesoporous Al–Ce–Cu oxide systems as catalysts for the preferential carbon monoxide oxidation (CO-PROX), *Catal. Commun.*, 2009, **10**, 522–527.

25 J. Cecilia, A. Arango-Díaz, J. Marrero-Jerez, P. Núñez, E. Moretti, L. Storaro and E. Rodríguez-Castellón, Catalytic Behaviour of CuO–CeO_2 Systems Prepared by Different Synthetic Methodologies in the CO-PROX Reaction under CO_2–H_2O Feed Stream, *Catalysts*, 2017, **7**, 160.

26 E. Moretti, A. I. Molina, G. Sponchia, A. Talon, R. Frattini, E. Rodriguez-Castellon and L. Storaro, Low-temperature carbon monoxide oxidation over zirconia-supported CuO–CeO_2 catalysts: Effect of zirconia support properties, *Appl. Surf. Sci.*, 2017, **403**, 612–622.

27 A. Corma, P. Atienzar, H. García and J. Y. Chane-Ching, Hierarchically mesostructured doped CeO_2 with potential for solar-cell use, *Nat. Mater.*, 2004, **3**, 394–397.

28 S. Xie, Z. Wang, F. Cheng, P. Zhang, W. Mai and Y. Tong, Ceria and ceria-based nanostructured materials for photoenergy applications, *Nano Energy*, 2017, **34**, 313–337.

29 S. S. Kim, S. J. Lee and S. C. Hong, Effect of CeO_2 addition to Rh/Al_2O_3 catalyst on N_2O decomposition, *Chem. Eng. J.*, 2011, **169**, 173–179.

30 F. Giordano, A. Trovarelli, C. De Leitenburg and M. Giona, A Model for the Temperature-Programmed Reduction of Low and High Surface Area Ceria, *J. Catal.*, 2000, **193**, 273–282.

31 R. Liu, H. Ye, X. Xiong and H. Liu, Fabrication of TiO_2/ZnO composite nanofibers by electrospinning and their photocatalytic property, *Mater. Chem. Phys.*, 2010, **121**, 432–439.

32 S. Hu, F. Zhou, L. Wang and J. Zhang, Preparation of Cu_2O/CeO_2 heterojunction photocatalyst for the degradation of Acid Orange 7 under visible light irradiation, *Catal. Commun.*, 2011, **12**, 794–797.

33 Y. Hua Xu, H. Rong Chen, Z. Xian Zeng and B. Lei, Investigation on mechanism of photocatalytic activity enhancement of nanometer cerium-doped titania, *Appl. Surf. Sci.*, 2006, **252**, 8565–8570.

34 F. B. Li, X. Z. Li, M. F. Hou, K. W. Cheah and W. C. H. Choy, Enhanced photocatalytic activity of Ce^{3+}–TiO_2 for 2-mercaptobenzothiazole degradation in aqueous suspension for odour control, *Appl. Catal., A*, 2005, **285**, 181–189.

35 U. Balachandran and N. G. Eror, Raman spectra of titanium dioxide, *J. Solid State Chem.*, 1982, **42**, 276–282.

36 R. D. Shannon and C. T. Prewitt, Effective ionic radii in oxides and fluorides, *Acta Crystallogr., Sect. B: Struct. Crystallogr. Cryst. Chem.*, 1969, **25**, 925–946.

37 L. Matějová, K. Kočí, M. Reli, L. Čapek, A. Hospodková, P. Peikertová, Z. Matěj, L. Obalová, A. Wach, P. Kuśtrowski and A. Kotarba, Preparation, characterization and photocatalytic properties of cerium doped TiO_2: On the effect of Ce loading on the photocatalytic reduction of carbon dioxide, *Appl. Catal., B*, 2014, **152–153**, 172–183.

38 P. E. Sobol, K. D. B. J. F. Moulder and W. F. Stickle, in *Physical Electronics Division*, ed. P.-E. C, Norwal, 1995th edn, 1995.

39 P. Georgios and S. M. Wolfgang, X-Ray Photoelectron Spectroscopy of Anatase-TiO_2 Coated Carbon Nanotubes, *Solid State Phenom.*, 2010, **162**, 163–177.

40 J. Lin, T. Sun, M. Li, J. Yang, J. Shen, Z. Zhang, Y. Wang, X. Zhang and X. Wang, More efficiently enhancing photocatalytic activity by embedding Pt within anatase–rutile TiO_2 heterophase junction than exposing Pt on the outside surface, *J. Catal.*, 2019, **372**, 8–18.

41 T. Tsoncheva, A. Mileva, G. Issa, M. Dimitrov, D. Kovacheva, G. Atanasova, J. Henych, V. Štengl, N. Scotti and M. Kormunda, Template-assisted hydrothermally obtained titania-ceria composites and their application as catalysts in ethyl acetate oxidation and methanol decomposition with a potential for sustainable environment protection, *Appl. Surf. Sci.*, 2017, **396**, 1289–1302.

42 E. Sheerin, G. K. Reddy and P. Smirniotis, Evaluation of Rh/$CexTi_{1-x}O_2$ catalysts for synthesis of oxygenates from syngas using XPS and TPR techniques, *Catal. Today*, 2016, **263**, 75–83.

43 T. Suwannaruang, J. P. Hildebrand, D. H. Taffa, M. Wark, K. Kamonsuangkasem, P. Chirawatkul and K. Wantala, Visible light-induced degradation of antibiotic ciprofloxacin over Fe–N–TiO_2 mesoporous photocatalyst with anatase/rutile/brookite nanocrystal mixture, *J. Photochem. Photobiol., A*, 2020, **391**, 112371.

44 M. Piumetti, S. Bensaid, N. Russo and D. Fino, Investigations into nanostructured ceria-zirconia catalysts for soot combustion, *Appl. Catal., B*, 2016, **180**, 271–282.

45 C. Dong, Z. Qu, Y. Qin, Q. Fu, H. Sun and X. Duan, Revealing the Highly Catalytic Performance of Spinel $CoMn_2O_4$ for Toluene Oxidation: Involvement and Replenishment of Oxygen Species Using in Situ Designed-TP Techniques, *ACS Catal.*, 2019, **9**, 6698–6710.

46 F. Mariño, C. Descorme and D. Duprez, Supported base metal catalysts for the preferential oxidation of carbon monoxide in the presence of excess hydrogen (PROX), *Appl. Catal., B*, 2005, **58**, 175–183.

47 B. Vijayan, N. M. Dimitrijevic, T. Rajh and K. Gray, Effect of calcination temperature on the photocatalytic reduction and oxidation processes of hydrothermally synthesized titania nanotubes, *J. Phys. Chem. C*, 2010, **114**, 12994–13002.

48 A. C. Johnston-Peck, S. D. Senanayake, J. J. Plata, S. Kundu, W. Xu, L. Barrio, J. Graciani, J. F. Sanz, R. M. Navarro, J. L. G. Fierro, E. A. Stach and J. A. Rodriguez, Nature of the mixed-oxide interface in ceria-titania catalysts: Clusters, chains, and nanoparticles, *J. Phys. Chem. C*, 2013, **117**, 14463–14471.

49 M. M. Khan, S. A. Ansari, D. Pradhan, D. H. Han, J. Lee and M. H. Cho, Defect-induced band gap narrowed CeO_2 nanostructures for visible light activities, *Ind. Eng. Chem. Res.*, 2014, **53**, 9754–9763.

50 S. A. Ansari, M. M. Khan, M. O. Ansari, S. Kalathil, J. Lee and M. H. Cho, Band gap engineering of CeO_2 nanostructure using an electrochemically active biofilm for visible light applications, *RSC Adv.*, 2014, **4**, 16782–16791.

51 J. J. Kim, S. R. Bishop, N. Thompson, Y. Kuru and H. L. Tuller, Optically derived energy band gap states of Pr in ceria, *Solid State Ionics*, 2012, 198–200.

52 A. H. Mahvi, M. Ghanbarian, S. Nasseri and A. Khairi, Mineralization and discoloration of textile wastewater by TiO2 nanoparticles, *Desalination*, 2009, **239**, 309–316.

53 A. Mills, C. Hill and P. K. J. Robertson, Overview of the current ISO tests for photocatalytic materials, *J. Photochem. Photobiol., A*, 2012, **237**, 7–23.

54 A. Houas, H. Lachheb, M. Ksibi, E. Elaloui, C. Guillard and J.-M. M. Herrmann, Photocatalytic degradation pathway of methylene blue in water, *Appl. Catal., B*, 2001, **31**, 145–157.

55 M. Basu, A. K. Sinha, M. Pradhan, S. Sarkar, A. Pal, C. Mondal and T. Pal, Methylene blue-Cu_2O reaction made easy in acidic medium, *J. Phys. Chem. C*, 2012, **116**, 25741–25747.

56 L. Jin, G. Sirigu, X. Tong, A. Camellini, A. Parisini, G. Nicotra, C. Spinella, H. Zhao, S. Sun, V. Morandi, M. Zavelani-Rossi, F. Rosei and A. Vomiero, Engineering interfacial structure in "Giant" PbS/CdS quantum dots for photoelectrochemical solar energy conversion, *Nano Energy*, 2016, **30**, 531–541.

57 W. Chewpraditkul, X. He, D. Chen, Y. Shen, Q. Sheng, B. Yu, M. Nikl, R. Kucerkova, A. Beitlerova, C. Wanarak and A. Phunpueok, Luminescence and scintillation of Ce^{3+}-doped oxide glass with high Gd_2O_3 concentration, *Phys. Status Solidi*, 2011, **208**, 2830–2832.

58 S. Kaniyankandy and H. N. Ghosh, Efficient luminescence and photocatalytic behaviour in ultrafine TiO_2 particles synthesized by arrested precipitation, *J. Mater. Chem.*, 2009, **19**, 3523–3528.

59 G. B. Vieira, H. J. José, M. Peterson, V. Z. Baldissarelli, P. Alvarez and R. de Fátima Peralta Muniz Moreira, CeO_2/TiO_2 nanostructures enhance adsorption and photocatalytic degradation of organic compounds in aqueous suspension, *J. Photochem. Photobiol., A*, 2018, **353**, 325–336.

60 Y. Li, Y. Fu and M. Zhu, Green synthesis of 3D tripyramid TiO_2 architectures with assistance of aloe extracts for highly efficient photocatalytic degradation of antibiotic ciprofloxacin, *Appl. Catal., B*, 2020, **260**, 118149.

61 L. Bergamonti, C. Bergonzi, C. Graiff, P. P. Lottici, R. Bettini and L. Elviri, 3D printed chitosan scaffolds: A new TiO_2 support for the photocatalytic degradation of amoxicillin in water, *Water Res.*, 2019, **163**, 114841.

62 Z. Xiu, Z. Xing, Z. Li, X. Wu, X. Yan, M. Hu, Y. Cao, S. Yang and W. Zhou, Ti^{3+}-TiO_2/Ce^{3+}-CeO_2 Nanosheet

heterojunctions as efficient visible-light-driven photocatalysts, *Mater. Res. Bull.*, 2018, **100**, 191–197.

63 L. T. T. Tuyen, D. A. Quang, T. T. Tam Toan, T. Q. Tung, T. T. Hoa, T. X. Mau and D. Q. Khieu, Synthesis of CeO_2/TiO_2 nanotubes and heterogeneous photocatalytic degradation of methylene blue, *J. Environ. Chem. Eng.*, 2018, **6**, 5999–6011.

64 W. S. A. El-Yazeed and A. I. Ahmed, Photocatalytic activity of mesoporous WO_3/TiO_2 nanocomposites for the photodegradation of methylene blue, *Inorg. Chem. Commun.*, 2019, **105**, 102–111.

65 A. Franco, M. C. Neves, M. M. L. R. Carrott, M. H. Mendonça, M. I. Pereira and O. C. Monteiro, Photocatalytic decolorization of methylene blue in the presence of TiO_2/ZnS nanocomposites, *J. Hazard. Mater.*, 2009, **161**, 545–550.

66 H. Feng, H. Xu, H. Feng, Y. Gao and X. Jin, The sol–gel synthesis and photocatalytic activity of Gd–SiO_2–TiO_2 photocatalyst, *Chem. Phys. Lett.*, 2019, **733**, 136676.

67 Z. Wei, M. Janczarek, M. Endo, K. Wang, A. Balčytis, A. Nitta, M. G. Méndez-Medrano, C. Colbeau-Justin, S. Juodkazis, B. Ohtani and E. Kowalska, Noble metal-modified faceted anatase titania photocatalysts: Octahedron versus decahedron, *Appl. Catal., B*, 2018, **237**, 574–587.

